

Supporting Information

Realizing both n- and p-types of High Thermoelectric Performance in $\text{Fe}_{1-x}\text{Ni}_x\text{TiSb}$ half-Heusler compounds

Nanhai Li^{a,b}, Huaxing Zhu^a, Wenlu He^a, Bing Zhang^c, Wenjun Cui^{d, e},
Zhi-Yi Hu^{d, e}, Xiahan Sang^{d, e}, Xu Lu^{*a}, Guoyu Wang^{*b}, Xiaoyuan
Zhou^{*a,c}

^aChongqing Key Laboratory of Soft Condensed Matter Physics and Smart Materials,
College of Physics, Chongqing University, Chongqing 401331, P. R. China

^bChongqing Institute of Green and Intelligent Technology, Chinese Academy of
Sciences, Chongqing 400714, P. R. China

^cAnalytical and Testing Center, Chongqing University, Chongqing 401331, P. R. China

^dState Key Laboratory of Advanced Technology for Materials Synthesis and
Processing, Wuhan University of Technology, 122, Luoshi Road, Wuhan, 430070, P.
R. China

^e Nanostructure Research Centre (NRC), Wuhan University of Technology, 122,
Luoshi Road, Wuhan, 430070, P. R. China

Contact Authors: luxu@cqu.edu.cn; guoyuw@cigit.ac.cn; xiaoyuan2013@cqu.edu.cn

1. Exploration of optimum ball milling time

As shown in Figure S2. (a) and (b), the Seebeck coefficient of $\text{Fe}_{0.5}\text{Ni}_{0.5}\text{TiSb}$ decreases as the ball milling time increases while the electrical conductivity is increased. However, it can be seen from the power factor that ball milling can seriously deteriorate the electrical performance of $\text{Fe}_{0.5}\text{Ni}_{0.5}\text{TiSb}$. In order to clarify the composition sensitivity for optimum ball milling time, the variation in electrical transport properties

with respect to ball milling time for different compositions has been investigated. For the samples with slight composition deviation from $\text{Fe}_{0.5}\text{Ni}_{0.5}\text{TiSb}$ ($\text{Fe}_{0.55}\text{Ni}_{0.45}\text{TiSb}$ and $\text{Fe}_{0.45}\text{Ni}_{0.55}\text{TiSb}$), the Seebeck coefficient drops and electrical conductivity increases with prolonged ball milling time seemingly due to defect induced carrier concentration change, finally leading to diminished power factor. In order to exclude the influence of carrier concentration, the material parameter quality β factor is introduced here. This parameter is defined by the relation^{1,2}:

$$\beta = \left(\frac{\kappa}{e}\right)^2 \frac{\sigma_0 T}{\lambda_L} \quad (1)$$

where κ is the Boltzmann constant, λ_L is the lattice thermal conductivity, σ_0 is a quantity termed as transport coefficient that depends on the carrier mobility and the effective mass according to:

$$\sigma_{E0} = 2e\mu \left(\frac{2\pi m_d^*}{h^2}\right)^{3/2} \quad (2)$$

where μ is the carrier mobility, m_d^* is the density of states (DOS) effective mass, h is the Planck constant. Clearly, the accurate calculation of σ_{E0} requires the information of mobility and m_d^* , which is time-consuming to access. Recently, Kang and Snyder developed a new approximation method to obtain σ_{E0} using just electrical conductivity and Seebeck coefficient independent of carrier concentration². The validity of this method was substantiated by a series of work³. Here, the method developed

by Snyder was employed to evaluate the effect of different milling time on the electrical properties of different Fe/Ni ratio samples, as displayed in Figure S3. (d). It can be clearly seen that the transport coefficient drops dramatically with ball milling time and the optimum ball milling time are 1.0 hour and 0.5 hour for $\text{Fe}_{0.55}\text{Ni}_{0.45}\text{TiSb}$ and $\text{Fe}_{0.45}\text{Ni}_{0.55}\text{TiSb}$, respectively. The reduced Seebeck coefficient can be ascribed to the increased carrier density, which results from defects generated during ball milling. However, the strengthened defect and boundary scattering for carriers does not allow for corresponding increase in electrical conductivity in these samples, in spite of enlarged carrier concentration.

Figure S4. (a-d) shows the effect of different ball milling time on the electrical transport properties of samples with large composition deviation from $\text{Fe}_{0.5}\text{Ni}_{0.5}\text{TiSb}$ ($\text{Fe}_{0.3}\text{Ni}_{0.7}\text{TiSb}$ and $\text{Fe}_{0.65}\text{Ni}_{0.35}\text{TiSb}$). For n-type $\text{Fe}_{0.3}\text{Ni}_{0.7}\text{TiSb}$, the Seebeck coefficient barely change with ball milling but electrical conductivity drops due to boundary scattering while the Seebeck coefficient of p-type $\text{Fe}_{0.65}\text{Ni}_{0.35}\text{TiSb}$ increases upon 3.0 hour milling. When checking the transport coefficient shown in Figure S4. (d), it is found that the intrinsic electrical performance of both $\text{Fe}_{0.65}\text{Ni}_{0.35}\text{TiSb}$ and $\text{Fe}_{0.3}\text{Ni}_{0.7}\text{TiSb}$ is superior to that of their counterparts with lower composition deviation, resulting from the band structure modification effect induced by the Fe/Ni ratio change. Interestingly, the transport coefficient of p-type $\text{Fe}_{0.65}\text{Ni}_{0.35}\text{TiSb}$ is improved by ball milling at both

room temperature and high temperature while that of n-type $\text{Fe}_{0.3}\text{Ni}_{0.7}\text{TiSb}$ is slightly diminished. Eventually, the optimum ball milling times are 3.0 hour and 1.0 hour for $\text{Fe}_{0.65}\text{Ni}_{0.35}\text{TiSb}$ and $\text{Fe}_{0.3}\text{Ni}_{0.7}\text{TiSb}$, respectively. The optimum ball milling time for the samples with varied compositions are listed in Table S2. Generally, it is concluded that the electrical transport properties of studied samples are sensitive to ball milling time and those with large composition deviation from $\text{Fe}_{0.5}\text{Ni}_{0.5}\text{TiSb}$ can endure longer ball milling time with little influence the electrical properties as they already have enough high carrier density. In contrast, the electrical transport property of the samples with small composition deviation and low carrier density is dramatically deteriorated due to the defect caused by ball milling.

2. Single parabolic band (SPB) model

The following equations are used to estimate the variation of effective mass when Fe/Ni ratio changes.

$$s = -\frac{k_B}{e} \left(\frac{\left(\frac{5}{2} + \lambda\right) F_{\frac{3}{2} + \lambda}(\eta)}{\left(\frac{3}{2} + \lambda\right) F_{\frac{1}{2} + \lambda}(\eta)} - \eta \right) \quad (3)$$

$$n_H = - \frac{4\pi(2m_d^*k_B T)^{\frac{3}{2}} F_{\frac{1}{2}}(\eta)}{h^3 r_H} \quad (4)$$

$$r_H = \frac{3}{2} \frac{F_{\frac{1}{2}}(\eta)}{F_{\frac{3}{2}+2\lambda}(\eta)} \frac{\left(\frac{3}{2} + 2\lambda\right) F_{\frac{1}{2}+2\lambda}(\eta)}{\left(\frac{3}{2} + \lambda\right)^2 F_{\frac{1}{2}+\lambda}(\eta)^2} \quad (5)$$

$$F_i(\eta) = \int_0^{\infty} \frac{x^i}{1 + \exp(x - \eta)} dx \quad (6)$$

where $\eta = E_F/k_B T$ is the reduced Fermi level, x is the reduced carrier energy, $F_i(\eta)$ is the Fermi-Dirac integral, r_H is the Hall factor, m_d^* is the density of states (DOS) effective mass, h is the Planck constant, and λ is the scattering factor which depends on the energy dependence of the carrier relaxation time τ via $\tau = \tau_0 \xi^\lambda$. When the acoustic phonon scattering or alloy scattering is dominant, $\lambda = -1/2$.

References

1. Goldsmid, H. J. *Thermoelectric Refrigeration* (Plenum, 1964).
2. S. D. Kang and G. J. Snyder, arXiv:1710.06896v2 [cond-mat.mtrl-sci] 2 Jan 2018.
3. S. D. Kang and G. J. Snyder, *Nature Materials*, 2017, 16, 252-257.

Figure Captions

Figure S1. X-ray diffraction patterns of $\text{Fe}_{1-x}\text{Ni}_x\text{TiSb}$ ($x = 0.40, 0.50, 0.55, 0.60, 0.65$) samples without ball milling.

Figure S2. Temperature dependence of the (a) electrical conductivity (solid square) and Seebeck coefficient (hollow square) (b) Power factor for $\text{Fe}_{0.5}\text{Ni}_{0.5}\text{TiSb}$ (ball milled for 2.0 hour, 1.0 hour, 0.5 hour and 0.2 hour).

Figure S3. Temperature dependence of the (a) electrical conductivity, (b) Seebeck coefficient, (c) Power factor (d) Transport coefficient for $\text{Fe}_{0.55}\text{Ni}_{0.45}\text{TiSb}$ (solid square) and $\text{Fe}_{0.45}\text{Ni}_{0.55}\text{TiSb}$ (hollow circle) (ball milled for 3.0 hour, 2.0 hour, 1.0 hour, 0.5 hour and 0 hour).

Figure S4. Temperature dependence of the (a) electrical conductivity, (b) Seebeck coefficient, (c) Power factor (d) Transport coefficient for $\text{Fe}_{0.65}\text{Ni}_{0.35}\text{TiSb}$ (solid square) and $\text{Fe}_{0.3}\text{Ni}_{0.7}\text{TiSb}$ (open circle) (ball milled for 3.0 hour, 2.0 hour, 1.0 hour).

Figure S5. SEM images of fresh fracture surface morphology of (a, b) $\text{Fe}_{0.5}\text{Ni}_{0.5}\text{TiSb}$ sample without ball milling and (c, d) $\text{Fe}_{0.5}\text{Ni}_{0.5}\text{TiSb}$ sample with 0.2 hour ball milling.

Figure S6. SEM images of fresh fracture surface morphology of (a) $\text{Fe}_{0.45}\text{Ni}_{0.55}\text{TiSb}$ sample with 0.5 hour ball milling and (b) $\text{Fe}_{0.55}\text{Ni}_{0.45}\text{TiSb}$ sample with 1.0 hour ball milling.

Figure S7. SEM images of fresh fracture surface morphology of (a) $\text{Fe}_{0.65}\text{Ni}_{0.35}\text{TiSb}$ sample with 3.0 hour ball milling and (b) $\text{Fe}_{0.7}\text{Ni}_{0.3}\text{TiSb}$ sample with 3.0 hour ball milling.

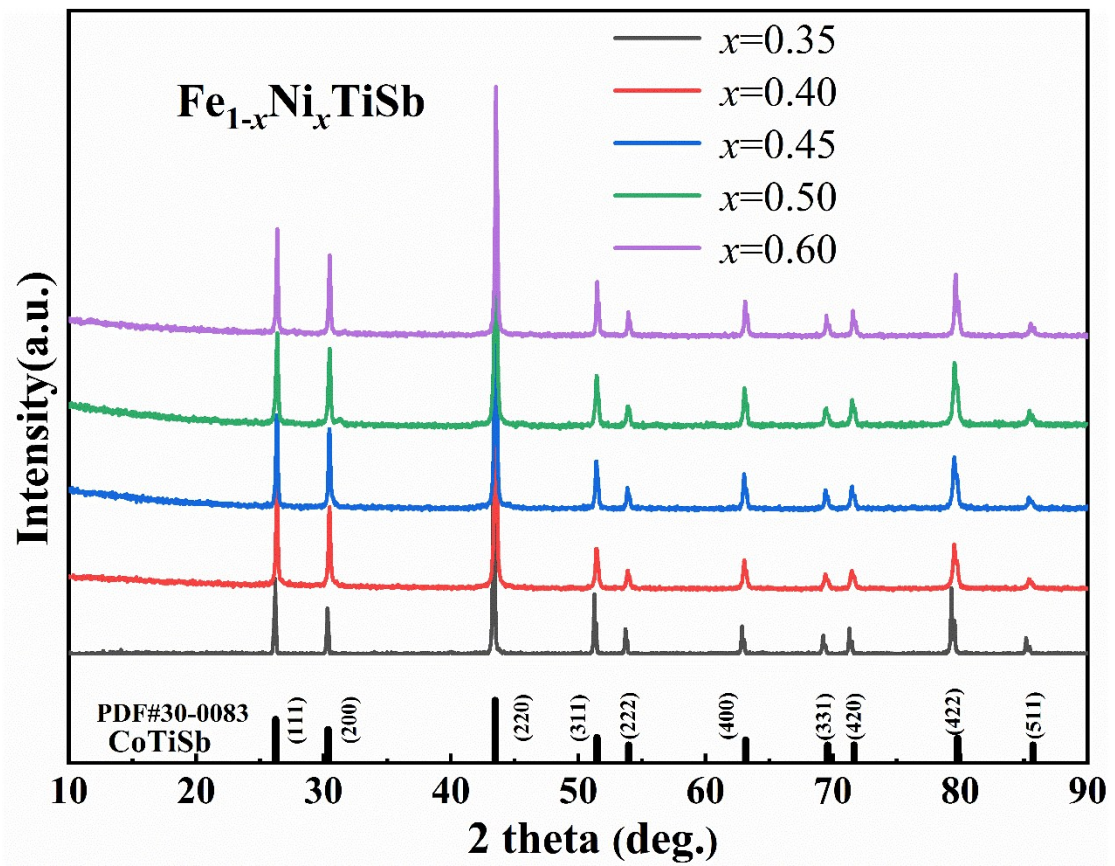


Figure S1. X-ray diffraction patterns of $\text{Fe}_{1-x}\text{Ni}_x\text{TiSb}$ ($x = 0.40, 0.50, 0.55, 0.60, 0.65$) samples without ball milling.

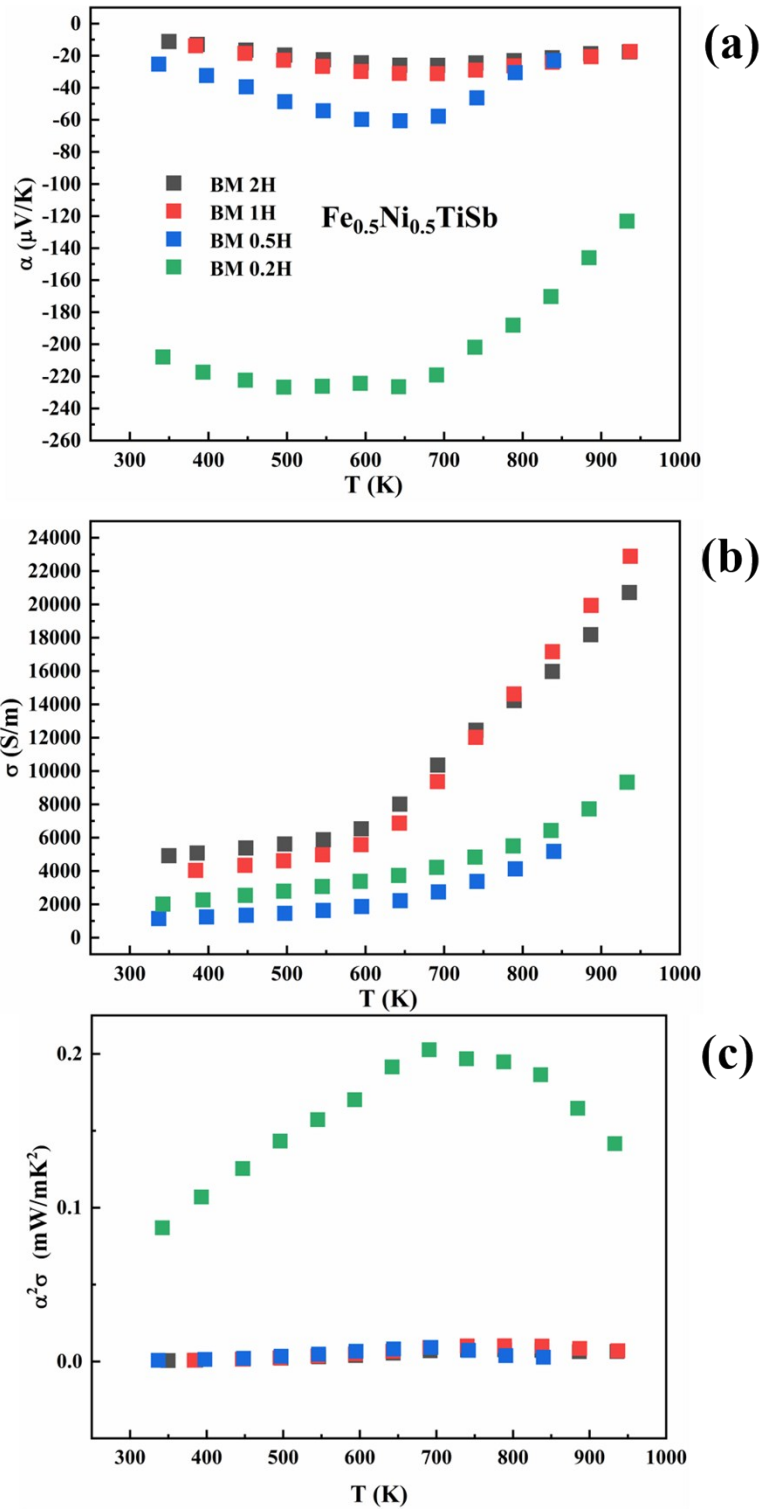


Figure S2. Temperature dependence of the (a) electrical conductivity (solid square) and Seebeck coefficient (hollow square) (b) Power factor for $\text{Fe}_{0.5}\text{Ni}_{0.5}\text{TiSb}$ (ball milled for 2.0 hour, 1.0 hour, 0.5 hour and 0.2 hour).

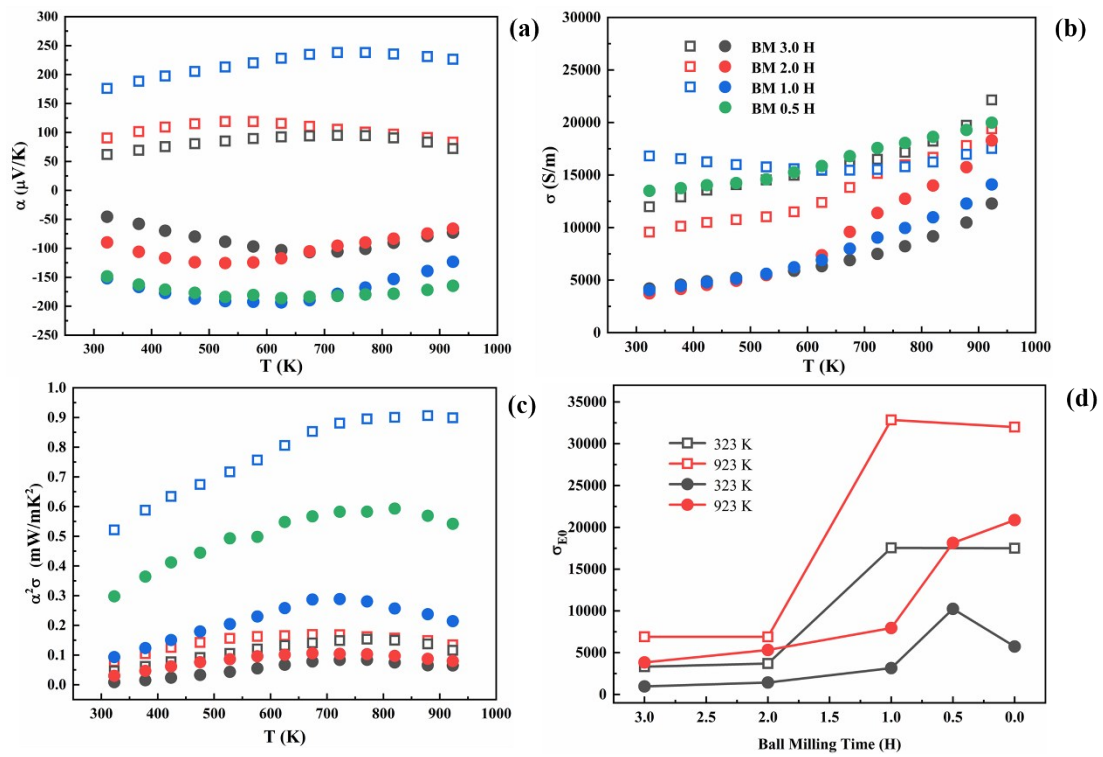


Figure S3. Temperature dependence of the (a) electrical conductivity, (b) Seebeck coefficient, (c) Power factor (d) Transport coefficient for Fe_{0.55}Ni_{0.45}TiSb (solid square) and Fe_{0.45}Ni_{0.55}TiSb (hollow circle) (ball milled for 3.0 hour, 2.0 hour, 1.0 hour, 0.5 hour and 0 hour).

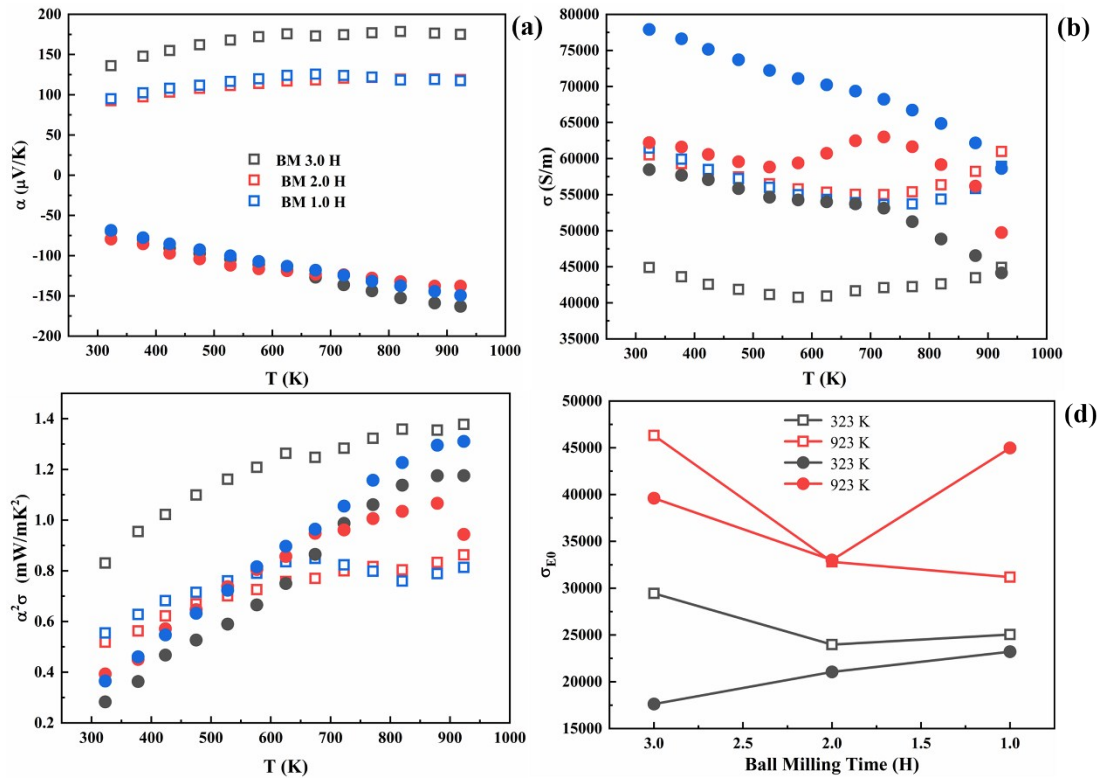


Figure S4. Temperature dependence of the (a) electrical conductivity, (b) Seebeck coefficient, (c) Power factor (d) Transport coefficient for $\text{Fe}_{0.65}\text{Ni}_{0.35}\text{TiSb}$ (solid square) and $\text{Fe}_{0.3}\text{Ni}_{0.7}\text{TiSb}$ (open circle) (ball milled for 3.0 hour, 2.0 hour, 1 hour).

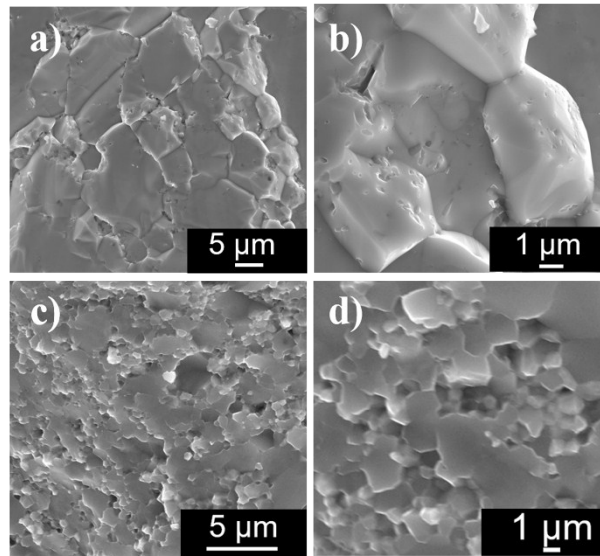


Figure S5. SEM images of fresh fracture surface morphology of (a, b) $\text{Fe}_{0.5}\text{Ni}_{0.5}\text{TiSb}$ sample without ball milling and (c, d) $\text{Fe}_{0.5}\text{Ni}_{0.5}\text{TiSb}$ sample with 0.2 hour ball milling.

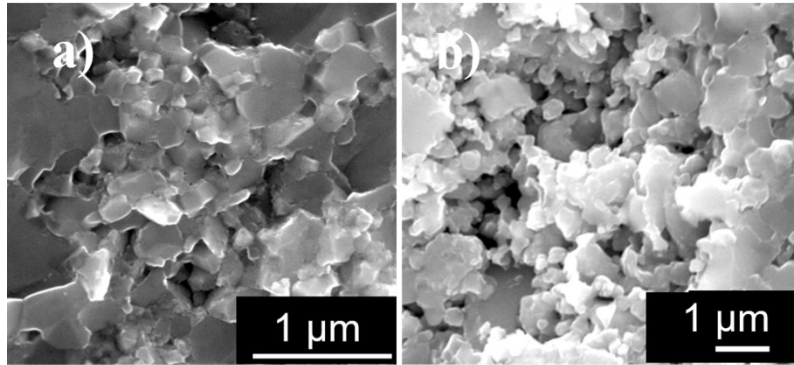


Figure S6. SEM images of fresh fracture surface morphology of (a) Fe_{0.45}Ni_{0.55}TiSb sample with 0.5 hour ball milling and (b) Fe_{0.55}Ni_{0.45}TiSb sample with 1.0 hour ball milling.

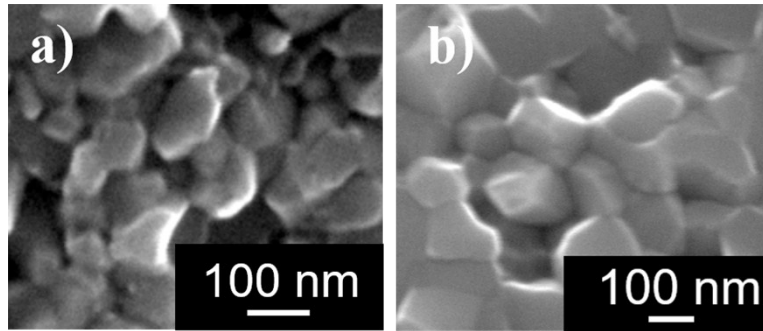


Figure S7. SEM images of fresh fracture surface morphology of (a) Fe_{0.65}Ni_{0.35}TiSb sample with 3.0 hour ball milling and (a) Fe_{0.7}Ni_{0.3}TiSb sample with 3.0 hour ball milling.

No.	Atom	Label	x	y	z	Occ.	B
1	Ti	Ti1	0.50000	0.50000	0.50000	1	1.3
2	Fe	Fe1	0.25000	0.25000	0.25000	0.65	0.66
3	Ni	Ni1	0.25000	0.25000	0.25000	0.35	0.36
4	Sb	Sb1	0.00000	0.00000	0.00000	0.92	0.2

Table S1. Structure parameters for $\text{Fe}_{0.65}\text{Ni}_{0.35}\text{TiSb}$.

Ni Content	0.30	0.35	0.40	0.45	0.50	0.55	0.60	0.65	0.70
Optimum ball milling time(h)	3.0	3.0	3.0	1.0	0.2	0.5	0.5	1.0	1.0

Table S2. Optimum ball milling time of $\text{Fe}_{1-x}\text{Ni}_x\text{TiSb}$ compounds with respect to Ni content.